Distributed Acoustic Sensing Along a Shallow Water Energy Cable

Nicholas Harmon, Mohammad Belal, Maria-Daphne Mangriotis, Carl Spingys, and Catherine A. Rychert

***Abstract*—Distributed acoustic sensing (DAS) provides a means of measuring dynamic changes in strain along a fiber-optic cable and has many potential applications for monitoring infrastructure, earthquake early warning, and hazard assessment. Previous work has focused on submarine telecommunications cables, which contain only fiber-optic cables. Here, we focus on the use of energy cables, which transmit electricity from offshore generators powered by tides or wind and contain fiber-optic cables for communications with the generators. Specifically, we focus on the European Marine Energy Center in Orkney, Eday, U.K., a tidal power station. Energy cables fluctuate in temperature due to energy transmission, and there is strong wave action and tidal flows, which all generate noise for DAS. We show that noise levels vary along the cable during a time with no energy transmission, but many phenomena reported on telecommunication cables are still observable, including ocean waves and nearby small vessels. The character of the small vessel signals in frequency band energy plots varies along the cable length, in some areas exhibiting multiple frequency band energy peaks. This variation is diagnostic of the burial state of the cable. Knowing the burial state of energy cables is important for understanding the mechanical protection of the system for minimizing thermal interactions with the surrounding environments and ecosystems (Lux et al., 2019).**

***Index Terms*—Optical fibers, optical fiber applications, underwater acoustics.**

I. Introduction

The advent of the use of submarine fiber-optic cables with distributed acoustic sensing (DAS) opens numerous possibilities for understanding the diverse range of biological, anthropogenic, oceanographic, and seismic signals that occur beneath the 70% of the planet covered by oceans. For example, DAS has been demonstrated to be useful for recording and tracking marine mammals in the Atlantic and Pacific Ocean Basins [2], [3], [4], [5]. Other studies have demonstrated the ability to track vessels and determine vessel noise characteristics [3], [5], [6], [7], [8]. A variety of oceanographic phenomena have also been studied using submarine DAS, ranging from locally generated and distant storm-generated surface gravity waves to tides [5], [8], [9], [10], [11], [12]. In addition, microseismic generation and manmade and natural seismic events have been observed using seafloor DAS [5], [8], [10], [13], [14], [15], [16], [17], [18].

Much of the previous work has used dark telecom fiber-optic links at tens of kilometers scale. However, undersea power cables that link offshore infrastructure such as wind or tidal turbines can also carry fiber-optic links [19]. Wind and tidal turbines are typically deployed in nearshore environments to minimize energy transmission loss and in locations with consistent wind speeds or strong tidal currents [20], [21], [22]. These cables provide an excellent opportunity for coastal environmental monitoring of oceanographic phenomenon and acoustic soundscapes. Due to the shallow water, cable design and deployment, and intrinsic thermal fluctuations due to electrical energy transmission, these fiber-optic links may be noisier than their telecommunications counterparts. However, it has been demonstrated that DAS using these types of cables can effectively record at least some of the aforementioned signals [6], [9]. In addition, usage on the fiber-optic cable is relatively low as they are typically only used for command and control of the offshore infrastructure.

Here, we examine the use of DAS on submarine power cables for subsea monitoring, specifically, the European Marine Energy Center (EMEC) in Orkney, Eday, U.K. (see Fig. 1) [23]. We demonstrate that low-frequency (<1 Hz) gravity waves can be observed as well as small vessels. We demonstrate that energy from small vessels in the near field of the cable can distinguish between the buried and unburied sections of the cable.

II. Methods

A. Site and Cable Description

The EMEC provides several test beds for new tidal and wave energy generators, with high-voltage cables equipped with fiber-optic cables also known as composite cables. The cables are comprised of three copper high-voltage alternative current power lines and a 12-core single-mode fiber-optic bundle [19]. The outer diameter of the cable is ~10 cm. The three conductors are near the axis of the cable, whereas the fiber-optic cables are

Received 28 April 2024; revised 28 October 2024; accepted 2 December 2024. This work was carried out by the National Oceanography Centre as part of project "SHARC: Submarine High-Fidelity Active-Monitoring of Renewable-Energy Cables," which was supported by UK Research and Innovation (UKRI) under Grant 77739. Some of the data preprocessing and analytics aspects of this work were also supported by UKRI under Grant NE/Y003365/1 and Grant NE/Z000408/1. *(Corresponding author: Nicholas Harmon.)*

Associate Editor: G. Potty.

Nicholas Harmon and Catherine A. Rychert are with the Woods Hole Oceanographic Institution, Woods Hole, MA 02543 USA, and also with the School of Ocean and Earth Science, University of Southampton, SO14 3ZH Southampton, U.K. (e-mail: nicholas.harmon@whoi.edu; catherine.rychert@whoi.edu).

Mohammad Belal is with the National Oceanography Centre, SO14 3ZH Southampton, U.K., also with the Department of Mathematical Science, University of Liverpool, L69 7ZL Liverpool, U.K., and also with the Department of Physics, University of Southampton, SO17 1BJ Southampton, U.K. (e-mail: mob@noc.ac.uk).

Maria-Daphne Mangriotis and Carl Spingys are with the National Oceanography Centre, SO14 3ZH Southampton, U.K. (e-mail: maria-daphne.mangriotis@noc.ac.uk; carl.spingys@noc.ac.uk).

Digital Object Identifier 10.1109/JOE.2024.3523363

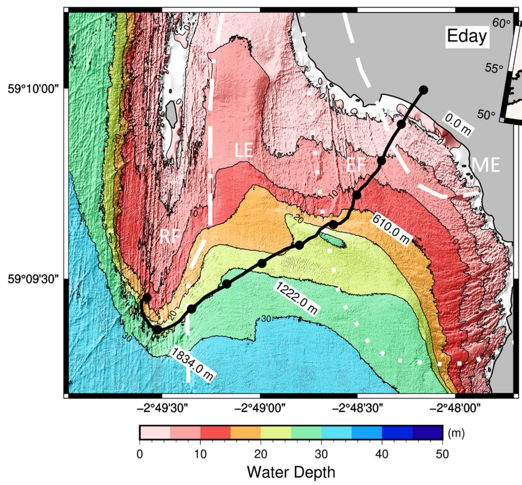

Fig. 1. Map of the study region offshore Eday Island, Orkney, U.K., with cable location. Colored and contoured bathymetric map of the region [24], with the cable shown by the thick black line. The gray colored region indicates land above the mean high tide. Labeled circles indicate the distance along cable used in subsequent figures. The dashed-dotted white line shows geologic boundary between Rousay Flagstones (RF, west) and Lower Eday Sandstone (LE). The dotted white line is the geologic boundary between Lower Eday Sandstone (west) and the Eday Flagstones (EF). The dashed white line shows the geologic boundary between the Eday Flagstones and the Middle Eday Sandstone (ME). The inset map shows the location of EMEC in the U.K., indicated with a yellow star.

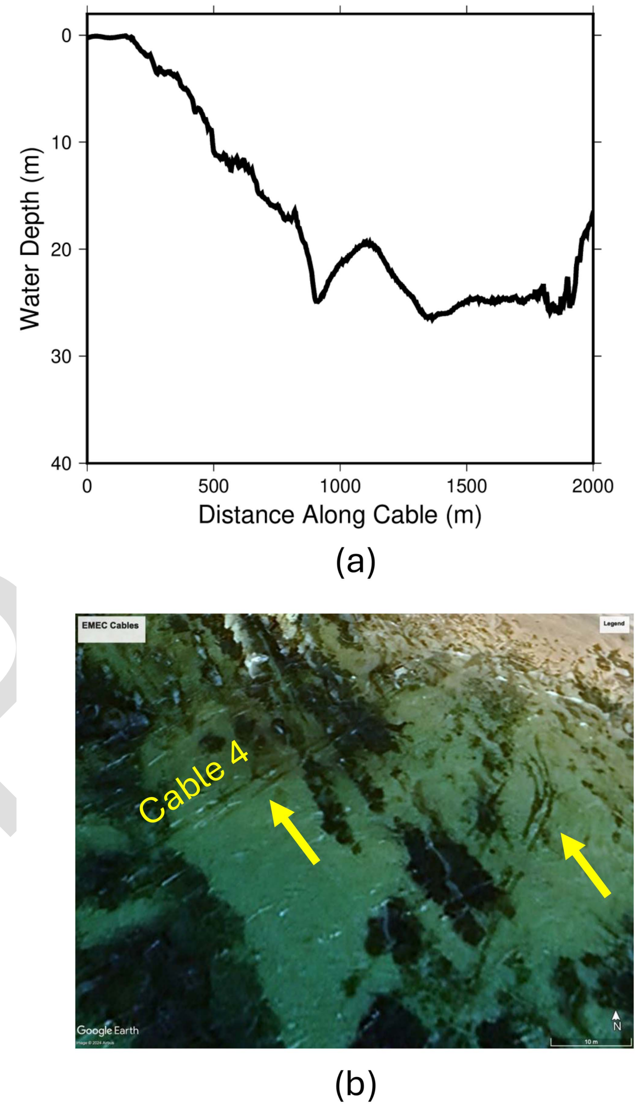

Fig. 2. Water depth and aerial photography of the cable on seafloor (a) Water depth along the cable distance. (b) Aerial photograph of the nearshore EMEC site from Google Earth/Airbus [25]. Yellow arrows indicate the locations of cables visible on the seafloor. Cable 4 is part of the northernmost cable group.

located near the outer radius of the cable. The cables are armored with two layers of steel wire. In shallow water (<15 m), the cables are also armored with ductile iron cable protectors. At the low tide mark, the cables are trenched underground until their final termination on land, but otherwise, the cables lie exposed on the seafloor [23]. In this study, we use Cable 4 at the Fall of Warness site (see Fig. 1), which has a strong tidal current, up to 7.8 kn (∼4 m/s) [23]. The cable location was digitized from maps of the cable location at the time it was laid on the seafloor. Therefore, there is some uncertainty in the cable location. A comparison of the digitized cable location with the location of the test bed site (where the cable should connect) and EMEC buildings in Google Earth/Airbus aerial photography [25] suggests that the error in location is on the order of ±20 m [see Fig. 2(b)].

The substrate of the cable varies along its length depending on local geology. The cable is located in the Eday Syncline, and variations in seabed geology are visible in the shaded bathymetry due to the variable competence of the rocks [26]. The westernmost portion of the cable lies within the variably grain-sized Rousay Flagstone unit, which is comprised of sandstones dipping to the east (west of the dashed-dotted gray line, Fig. 1). The bathymetry beneath this unit is defined by several north–south trending scarps caused by the bedding planes. Immediately adjacent to the east is the fine-grained Lower Eday Sandstone (between the gray dashed-dotted and gray dotted lines, Fig. 1), which has been eroded to form a local embayment and beach. Bathymetric fabric above this unit is smoother in character, partly due to eroded sands covering the unit. Sand ripples are visible in some parts of this unit (north of the 1220.2 m label, Fig. 1) and scour depressions in other parts due to high tidal velocities. Further east are the Eday Flagstones comprised of some volcanic layers and siltstones/sandstones (between the dashed and dotted lines, Fig. 1) and the medium grain-sized Middle Eday Sandstones (east of the dashed line). The bathymetric character of these two units is similar to the Rousay Flagstones, with scarps due to bedding that curve around to the south, near the nose of the syncline. Visual inspection of aerial imagery over the site [see Fig. 2(b)] shows that the cables are exposed on the seabed lying on top of the bed scarps of the Upper Eday Sandstones and Eday flagstones for ∼100 m where the bottom is visible.

B. Acquisition Parameters

The data used in this work were obtained using a DAS system based upon the differential Rayleigh phase-based approach (*d*&PHgr;-DVS) [27], developed as part of the National

Oceanography Centre (NOC, Southampton, U.K.) intelligent marine fiber sensing research program. The data were acquired using offsite interrogation of the system physically connected to the shore end of ∼2 km offshore seafloor energy cable. The field campaign was conducted in November 2020. The data were acquired with a gauge length of 10 m and spatially sampled at 2.04 m along the cable. The sampling frequency was 1000 Hz, with the optical probing routine set to use a single-probe frequency. There was no energy transmission during the recording period of our experiment.

C. Data Processing, Frequency Band Energy, and Spectral Analysis

We present low-frequency DAS signals to highlight oceanographic signals. We detrend and demean the time series. We lowpass filter using a fourth-order Butterworth zero-phase filter with a cutoff at 0.5 Hz.

We use frequency band energy (FBE) plots to identify small vessels passing near the cable. FBE is a summation across the power spectral density (PSD) of a selected discrete frequency band, with the PSD representing the power content versus frequency, which is often used to characterize random processes [28]. FBE analysis has been used in cosmology for applications such as cosmic microwave background separation from foreground noise [29] and analysis of cosmological temperature and polarization anisotropies [30], with a view to fundamentally isolate the signals from distant astrophysical sources and/or large-scale structure formation. We calculate the FBE plots in the following way. We first detrend the data and then use an eighth-order Butterworth zero-phase bandpass filter between 60 and 80 Hz, which encompasses the strongest peak in the signal from the small vessel. We then calculate the running median of the envelope of each trace over a 2- or 5-s window, chosen to enhance presentation at different scales. The envelope is calculated using the absolute value of the complex Hilbert transform pair. The centroid of the energy of the FBE along the fiber provides an approximate location of the small craft at any given time. The rate of change of the centroid along the fiber provides an approximate velocity.

Spectrograms of the traces over different frequency bands are used to explore time variations in the signals of the small vessels. Spectrograms are calculated using short-time Fourier transforms. A frequency resolution of 0.25 Hz is used with a ∼10 s Hanning window with 80% overlap. We present estimates of predicted Doppler shifts based on the frequency with the maximum power in the spectrogram. We use the following equation:

$$f_O = \frac{c_{\text{water}}}{c_{\text{water}} + \boldsymbol{r} \cdot \boldsymbol{v_s}} f_s \tag{1}$$

where f_O is the observed frequency at a fixed point on the cable, f_S is the frequency emanating from the source, and c_{water} is the speed of sound in water (1500 m/s), $\boldsymbol{r}$ is the vector between the source and the observed location, and $\boldsymbol{v_s}$ is the velocity vector of the source, or small craft. In addition to the spectrograms, we measure the Doppler shift using the change in instantaneous frequency calculated from the Hilbert transform described previously, which is used in the FBE plots.

D. Coupled Versus Uncoupled Fiber Response

The stress and strain on a fiber that result from an impinging plane pressure wave are expected to vary depending on the properties of the medium(s) surrounding the fiber. For instance, the cable may be surrounded by the water column or buried or coupled to the Earth. In the water column, only normal stresses due to pressure variations can cause strain on the cable as shear is not supported. In contrast, a buried cable is subjected to both shear and normal stresses. The stress and strain response of the medium surrounding the cable can be determined from the elastic wave equation and Hooke's law.

For a 1-D liquid–solid boundary, the following boundary conditions apply: normal stress is continuous at the boundary, shear stress disappears at the boundary, and normal displacements are continuous at the boundary. We define a 2-D coordinate system $x_{1,3}$, where direction 1 is horizontal (in line with the fiber) and direction 3 is vertical. We assume that the boundary is at $x_3 = 0$ for convenience. The fluid density (&rgr;^{f}) and P-wave velocity (v_p^f) are indicated by a superscript f, whereas the solid earth half-space P-wave velocity (v_p), S-wave velocity (v_s), and density (&rgr;) are not superscripted. The incidence angle θ is relative to the vertical direction (x_3). At a fluid–solid boundary, there are three waves generated by the incident P-wave in the water: the reflected P-wave, the transmitted P-wave, and the transmitted S-wave. We define the foll*owing* parameters for these waves:

$$p = \frac{\sin\theta}{v_p^f} \tag{2}$$

where p is the horizontal slowness of the incident P-wave and is the same for all waves

$$\eta^f = \frac{\cos\theta}{v_p^f} = \sqrt{\frac{1}{{v_p^f}^2} - p^2} \tag{3}$$

where η^f is the vertical slowness of the incident P-wave

$$\eta = \sqrt{\frac{1}{v_p^2} - p^2} \tag{4}$$

where η is the vertical slowness of the transmitted P-wave

$$\eta_S = \sqrt{\frac{1}{v_s^2} - p^2} \tag{5}$$

where η_s is the vertical slowness of the transmitted S-wave.

We also define a denominator for the reflection and transmission coefficients, as follows:

$$D = \eta^f \left(-\left(p^2 - \eta_s\right)\left(\rho - 2\rho v_s^2 p^2\right) + 4\rho v_s^2 p^2 \eta \eta_S \right) + \frac{\rho^f \eta}{v_S^2}. \tag{6}$$

The P-wave reflection coefficient (subscripts denote P incoming and either P or S outgoing) for an incident wave with amplitude A_0 (in square meters) is

$$R_{PP} = \frac{\eta^f\left(-\left(p^2-\eta_s\right)\left(\rho-2\rho v_s^2p^2\right)+4\rho v_s^2p^2\eta\eta_S\right)-\frac{\rho^f\eta}{v_S^2}}{D}A_0. \tag{7}$$

The transmitted P-wave is given by

$$T_{PP} = \frac{2\rho^f\eta^f\left(p^2-\eta_S^2\right)}{D}A_0. \tag{8}$$

The transmitted S-wave coefficient is given by

$$T_{PS} = \frac{4p\eta\eta^f}{D}A_0. \tag{9}$$

The displacements in the solid as a function of frequency at $x_3 = 0$ are given by

$$u_1\ (\omega, x_1, p) = \ i\omega\exp\left(i\omega\left(px_1\right)\right)\left(pT_{PP}+\eta_ST_{PS}\right) \tag{10}$$

$$u_3\ (\omega, x_1, p) = \ i\omega\exp\left(i\omega\left(px_1\right)\right)\left(\eta T_{PP}+pT_{PS}\right). \tag{11}$$

Strain in direction 1 in the solid substrate is given by

$$\varepsilon_{11} = \ -\omega^2\mathrm{p}\exp\left(i\omega px_1\right)\left(pT_{PP}+\eta_ST_{PS}\right). \tag{12}$$

Pressure in the water at the interface is given by

$$P\ (\omega, x_1, p) = \ \omega^2\rho^f\exp\left(i\omega px_1\right)\left(R_{PP}+A_0\right). \tag{13}$$

The formulations from [31] show that a linear relationship between inline strain ε_{11} due to hydrostatic pressure on a two-layer cable is given by

$$\varepsilon_{11} = \frac{1-2\left(1-f\right)\sigma_g-2f\sigma_p}{fE_g+\left(1-f\right)E_p}P \tag{14}$$

where E_g and E_p are the Young's moduli of the glass fiber and plastic casing, respectively, and σ_g and σ_p are the Poisson's ratios of the glass and plastic coating, respectively. The square of the ratio of the glass fiber to plastic casing radii is given by f.

The strain on the cable in response to a source with changing incidence angle is expected to be very different if it is in the water (13) or buried (12). If the cable is in the water, the energy on the cable should be high at zero incidence angle. Conversely, if the cable is coupled to the seafloor, its sensitivity should be zero at zero incidence angle and should increase as the incidence angle moves away from zero. In this article, we are not focused on the absolute values of strain, but on the relative response between a cable in the water and one just beneath the fluid–solid interface. However, for illustrative purposes, we compare the predicted pressure in the water and the predicted strain in the solid and the strain caused by quasi-hydrostatic loading of the fiber [31] as a function of incidence angles (see Fig. 3). We assume the following parameters in the plot: $v_p = 2000$ m/s, $v_s = 1000$ m/s, $\rho = 2000$ kg/m^3, $v_p^f = 1500$ m/s, $\rho^f = 1000$ kg/m^3, $\omega = 2*\pi*70$ Hz, $E_g = 64\mathrm{e}9$ Pa, $E_p = 0.76\mathrm{e}9$, $v_g = 0.24$, and $v_p = 0.4$. We assume $f << 1$ in these calculations with a 6-μm fiber and a 2-cm plastic coating.

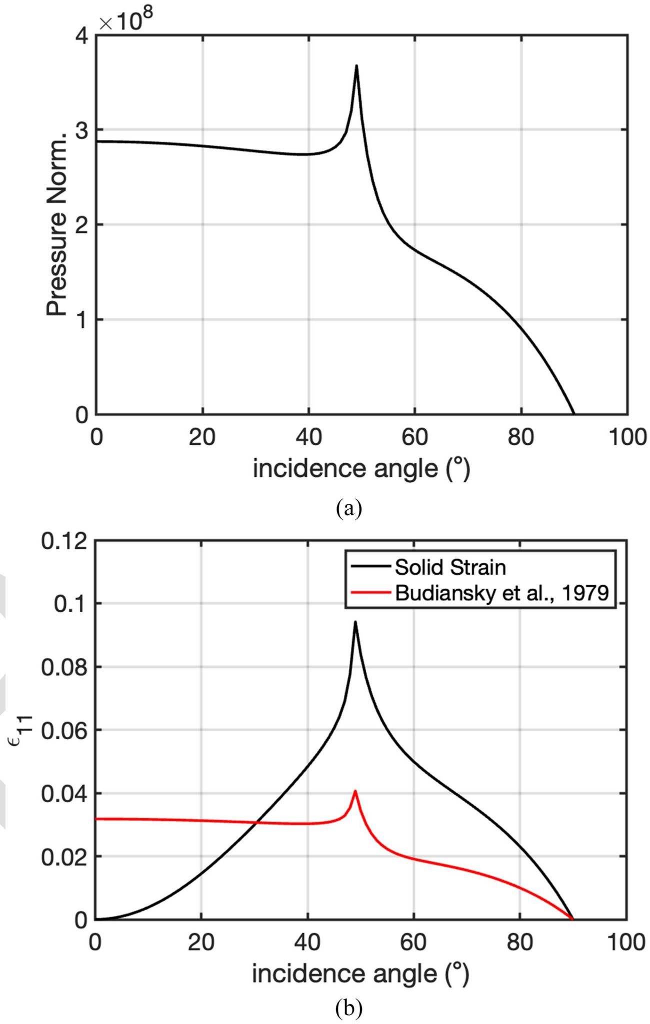

Fig. 3. (a) Predicted pressure. (b) Predicted inline strain. In (b), the red line shows the strain predicted for a cable in the water column using the relationship presented by Budiansky et al. [31] to convert pressure to inline cable strain. The black line is the predicted strain in a solid (earth) as a function of incidence angle.

III. Results

A. Oceanographic and Small Vessel Signals

Time series at different locations along the cable show clear and coherent signals across a wide frequency range along the length of the cable (see Fig. 3). At low frequency, a 0.08-Hz (∼12 s) signal is visible from the distance of approximately 900–1800 m along the cable, with an apparent moveout of ∼17 m/s, and from the distance of 20–500 m with a slower moveout of ∼10 m/s [see Fig. 4(a)]. The strength of this signal varies along the distance of the fiber, with 20–500 and 900–1400 m having particularly high-amplitude signals. These signals have a moveout and frequency consistent with shallow water ocean surface gravity waves. In addition, around ∼400 s at ∼1100 m, a coherent wave train with the opposite sense of moveout is visible, cutting across the incoming wavefield, which is consistent with reflected ocean gravity waves [see Fig. 4(a)].

In the high-frequency FBE plot [see Fig. 4(b)], a narrow (10–30 s) region of high energy (black region) with a moveout of 10–11 m/s is visible between 1800 and 100 m distance along the cable from 100 to 300 s and with an opposite moveout from 300 to 500 s. This signal was generated by a small vessel that steamed along the cable length in opposite directions during

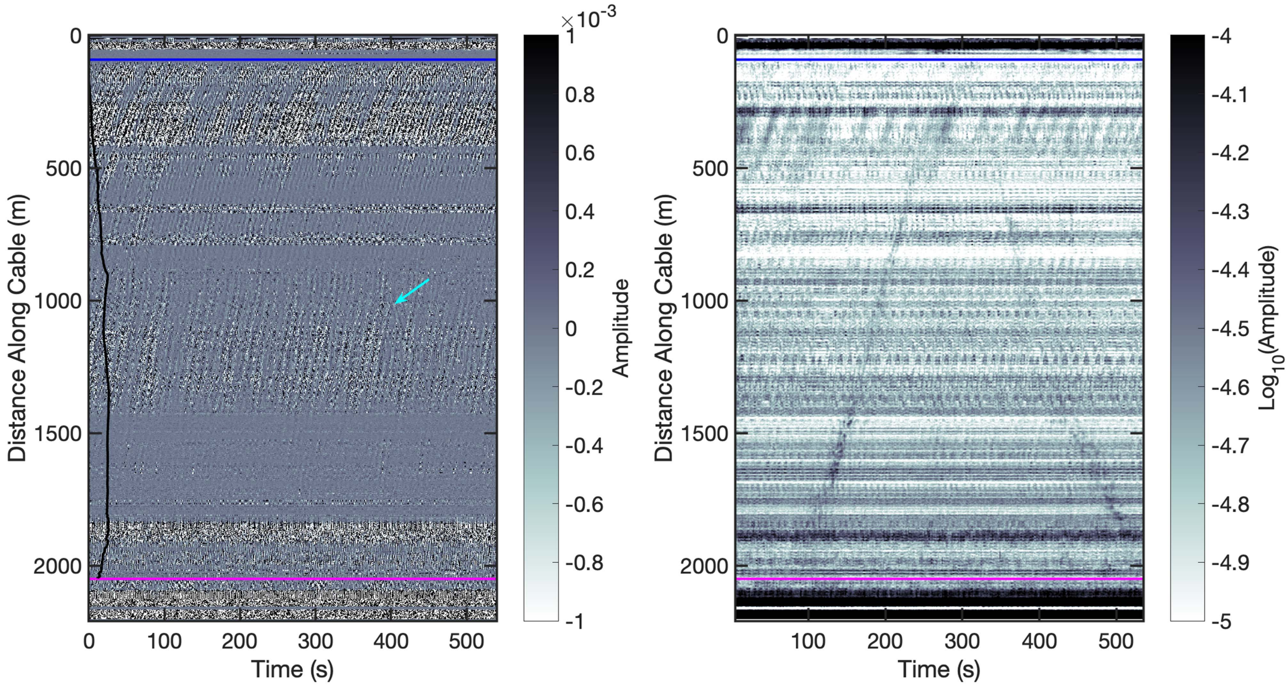

(a) (b)

Fig. 4. Time series over the length of the cable. (a) Lowpass-filtered time-series data at 0.5 Hz. The cyan arrow indicates the location of one refection with an opposite moveout. (b) FBE plot of energy from 60 to 80 Hz bandpass-filtered data showing a small craft passage at ∼10 m/s. The recording time starts on 12 November 2020, 09:16:01.5 GMT. The blue line indicates the land–ocean boundary of the cable, while the magenta line indicates the transition from the ocean to the turbine platform. The thick black line in (a) illustrates variation in water depth along the cable, with units of meters (1 m = 1 s on the time axis).

the experiment. The vessel was the MV C-Spartan, which is 12 m in length with a 0.8-m draught and a maximum speed of 18 m/s (35 kn). Again, the signal visibility varies along the length of the cable. In contrast to the low-frequency signals, the high-frequency signals have higher amplitude from 1400 to 1800 m along the cable and are muted elsewhere. Both the low- and high-frequency plots do not have visually coherent signals where the cable changes the direction sharply, e.g., ∼ 650, 830, and 1834 m. In addition, there is a beating pattern of alternating high and low FBE values, which have a similar moveout to ∼12 s ocean gravity waves.

The average power (modulus of square amplitude) varies along the cable length and shows systematic variations in different frequency bands (see Fig. 5). We show examples from two frequency bands of interest, low frequency (<0.5 Hz) to quantify energy changes in ocean gravity wave signals, and high frequency (68–78 Hz) to highlight small craft detectability. We present the average power over a 1-min window that included ship tracks [see Fig. 5(a) and (b)]. The power is similar in both plots (10–10^3), with both having maxima near 0 m and >2000 m. The maxima are likely the result of increased strain related to the cable hanging from connection points at its endpoints. At low frequencies, power is relatively high (10^3) from a distance of 100–500 m, where the water depth is <10 m. It also reaches similar values around ∼650 m and ∼770 m, where the cable changes orientation around a small diversion in the cable. There is also another broad peak from 1000 to 1300 m (10^3), which is likely related to the favorable slope orientation (dipping toward the incoming waves). The peak is centered on the middle of the shallowing water depth in the 1100–1300 m cable distance range. There are low values (10^1–10^2) from ∼1430 to 1817 m, where the bathymetry is relatively flat, smooth, and likely sandy. In the unnormalized high-frequency power plot, the power is relatively consistent at $\sim 10^3$. Power plots normalized by the average power at all frequencies (zero to Nyquist) for each trace are shown for low frequency [see Fig. 5(c)] and high frequency [see Fig. 5(d)]. For low frequency, very little change is observed in the power along the cable in comparison to the unnormalized case. However, at high frequencies [see Fig. 5(d)], differences between the unnormalized power are visible, particularly from 1450 to 1700 m, the power is higher (0.020) than most of the rest of the line (0.002–0.01). In other words, normalization highlights the region where the ship signal is highest in the FBE plots. In this same region, the wave signal power is lower.

The Doppler shift of the small vessel engine signal is visible in spectrograms and in instantaneous frequency plots (see Fig. 6). The Doppler shift is particularly pronounced along the moveout of the boat [10 m/s, high amplitudes with a similar slope as the white line, Fig. 6(a) and (b)]. The small vessel traversed along the line of the cable. The shift in frequency ranges from 71.6 to 70.6 Hz with increasing time, which is in good agreement with predictions from (1) [see Fig. 6(c)–(e)] for a path that is aligned parallel to the fiber. The energy in the spectrograms is not constant as the frequency changes, and it is not necessarily at a maximum when the small vessel is closest to the fiber. Rather, some traces have more energy at the extreme values of

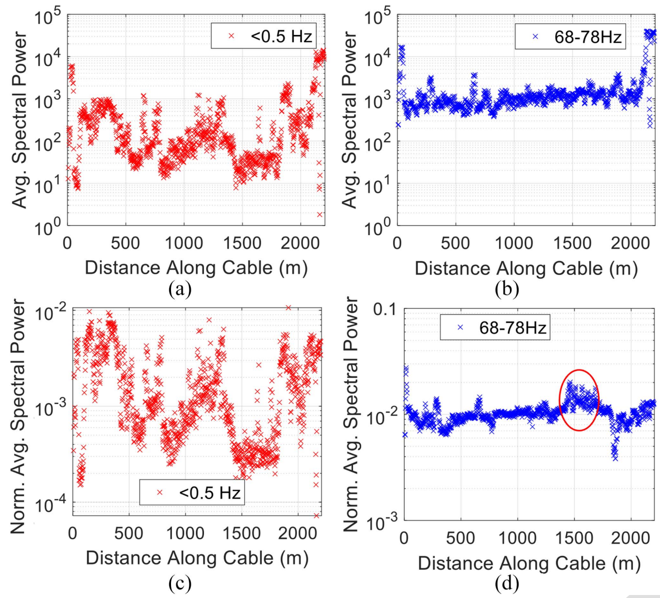

Fig. 5. Averaged power of phase difference. The (a) low-frequency range (up to 0.5 Hz) and (b) frequency range of 68–78 Hz over a 1-minute phase difference window that included ship tracks are shown. (c) and (d) are the same but normalized using the average of all frequencies. Note that the ship track signature [red circle in (d)] is only observed in the narrowband 68–78 Hz, after normalization by the average power.

the Doppler shift frequency range, particularly at 1572 m [see Fig. 6(d)]. This is likely primarily related to the inline response of fiber-optic cables with some contributions from interference effects due to the scattering of acoustic energy. The FBE plot shows that there are also several discrete packets of high amplitude for some traces at a given distance along the cable, while other traces only show a single peak in energy, for example, at 1389 m [see Fig. 6(c)–(e)]. This change in character in the FBE plots may be related to variations in the coupling of the cable, which we explore later. The instantaneous frequency plot [see Fig. 6(b)] shows a relatively wide-banded transition from 71.6 to 70.6 Hz (change in color from yellow/orange to green with increasing time), where the FBE energy is high between 1425 and 1580 m, while outside of this range, the difference in frequency range of the Doppler shift is more muted, i.e., a band at 70.25 Hz is visible (green only), typically where only a single packet of energy is visible in the individual traces in the FBE. The range of the Doppler shift we observe, from 71.6 to 70.6 Hz, would yield a source velocity of ∼10 m/s, which is generally consistent with the apparent velocity measured on the FBE [10-m/s line, Fig. 6(a) and (b)].

B. Modeling of Cable Response to a Small Vessel Source

To illustrate the effects of a moving source on a buried and unburied cable, we generate a simple model for the cable's response to the source in the water column and within the seafloor. The source emits a constant frequency of 70 Hz signal and travels at 10 m/s. The source is located 30 m above the receiver cable and travels inline along the cable [see Fig. 7(a)] for 200 m. To simulate revving of the engine as the vessel pushes through swell, we added a 12-s period amplitude modulation to the signal. We assume a point source and calculate the predicted pressure at the seafloor (11), as well as the predicted strain in the solid part of the seafloor (12). We compare the predictions for FBE plots [see Fig. 7(b) and (c)] to the data [see Fig. 7(d) and (e)]. The FBE plots in Fig. 7 are time shifted by the moving source's speed and summed in the subpanels of Fig. 7 to illustrate the simplified pattern of energy relative to the source's position or incidence angle.

The synthetic examples show distinct patterns in the FBE plots. The buried synthetic FBE generates two maxima, with a minimum energy level in between, centered where the small craft is directly overhead [see Fig. 7(b)]. This is because of its sensitivity to ε_{11} in the inline direction of the fiber. When the small vessel is above the fiber, it generates little to no ε_{11} strain, whereas at other distances/times, there is an increase in amplitude leading up to the critical angle where refraction occurs. The amplitude modulation we apply to simulate engine revving through swell varies the amplitude, producing a diagonal striping in the shifted synthetic FBE plots. The summed FBE plot for the buried synthetic shows the two maxima clearly at ∼7.5 and 12. 5 s [see Fig. 7(b)]. For the unburied synthetic, there is only a single maximum generated, beneath where the small craft is overhead [see Fig. 7(c)]. There is also diagonal striping visible in the FBE plots caused by the engine revving amplitude modulation [see Fig. 7(c)]. The single peak is visible in the summed FBE [see Fig. 7(c)]. In this case, the pressure signal is greatest at normal incidence, and the small vessel's proximity to the cable causes ε_{11} strain. The lack of coupling results in a scenario where pressure is proportional to ε_{11} strain.

The observation shows FBE patterns similar to the synthetics for both the buried and unburied cases. For example, for the cable between 1500 and 1600 m distance, a broad region of energy is visible in the FBE plot from 137 to 152 s [see Fig. 7(d)], which when summed results in two peaks at 142 and 148 s [see Fig. 7(d)]. This is like the synthetic buried case [see Fig. 7(b)]. For the cable between 650 and 750, the FBE peak energy is in a narrower region between 222 and 227 s [see Fig. 7(e)], which when summed produces a single strong peak at 226 s [see Fig. 7(e)]. This is similar to the synthetic unburied case's single peak [see Fig. 7(c)].

IV. Discussion

Submarine energy cables can be used to observe a broad spectrum of signals. At low frequency (<0.5 Hz), ocean surface gravity waves are observed across the entire cable [see Fig. 4(a)]. The observed velocity of 9.9–17.2 m/s is consistent with phase velocities for shallow water waves. For shallow water, where the water depth is less than half a wavelength, the surface gravity wave phase speed is given by $c = \sqrt{gh}$ [32], which in this case implies speeds of 17.2 m/s for the offshore locations and 9.9 m/s for the nearshore case. The presence of these surface gravity waves also implies that oceanographic signals will be present at higher frequencies as these waves undergo nonlinear wave breaking and a downscaled turbulent energy cascade [33]. This range of processes results in a higher noise floor from the

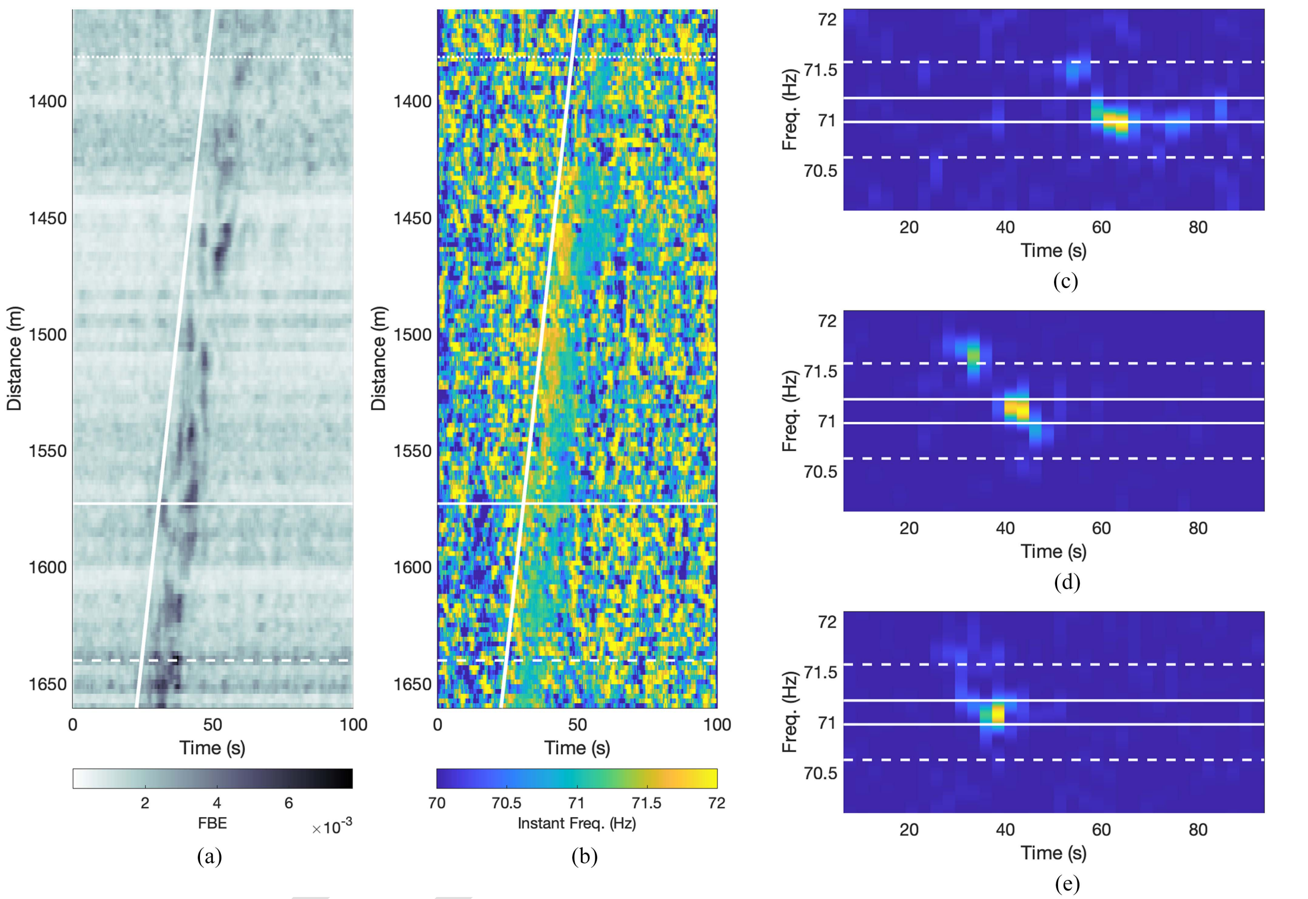

Fig. 6. Doppler shift observations of small craft passing over the cable. (a) Close-up view of FBE from 1360 to 1660 m. The start time of the plot has been arbitrarily set to 0. Horizontal white lines indicate the locations of traces used in (c)–(e), while thick white lines indicate a moveout of 10 m/s. (b) Instantaneous frequency of the traces from 1360 to 1660 m. White lines same as in (a). Spectrograms of individual traces at (c) 1639 m, (d) 1572 m, and (e) 1389 m. White dashed lines indicate a predicted Doppler shift for 10 m/s and white solid lines indicate a Doppler shift for 2.5 m/s for a center frequency of 71.14 Hz.

wave frequency to Kolmogorov scales where viscosity damps the turbulent motions, typically O(1 mm) length scale, which, combined with background flow advection of O(1 m/s), implies a frequency of O(1000 Hz) for a fixed position in this environment. At higher frequencies, >10 Hz, the background in the FBE plots exhibits a beating pattern of high and low energy with a period of ~12 s (Fig. 4(b), 200–500 m), which is likely related to the turbulent energy cascade. In addition, the nearby small vessel is observed. Given the nature of the cable, specifically that it is designed for energy transfer, laid out on the seafloor over a variably rocky substrate, and in a strong tidal-shallow water environment, it is remarkable that these signals are visible.

Our observations of incoming and reflected ocean gravity waves at low frequencies are in line with several previous studies that also observed ocean gravity waves using telecommunications and power cables. For example, shallow water dark communication cables were used to observe ocean gravity waves offshore Belgium and were able to observe both incoming and shore reflected waves using a chirped pulse DAS setup [16]. Our ability to observe the ocean gravity waves opens the potential for investigations of nearshore currents using Doppler shifts in the wave periods from beamforming, as has been demonstrated offshore Gibraltar on a power cable in 0–150 m water depth [9]. Weak reflections from the shorelines observed here were also observed in other shallow water time series and frequency wave number plots [9]. Because our cable is in relatively shallow water (<30 m), it is expected that pressure signals from ocean gravity waves should be visible at almost all frequencies where the wavelength is larger than the gauge length. Other studies in greater water depths using bottom pressure records typically detect only low-frequency infragravity waves, as expected due to the frequency-dependent decay of a wave's pressure with depth [34], [35], [36], [37]. Several other studies have also observed ocean gravity waves locally and from distant storms, determined from long time series and observed dispersion of the wave field over days [5], [8], [10], [11], [15]. Our time series were not long enough to assess the capability of the cable for this type of work.

Our work is also in line with previous work, which has observed acoustic sources from vessels and marine life [2], [3], [4], [5], [6], [7], [13], [17]. In comparison with previous work, the detection range of the small vessel in our region is limited to <200 m of the cable at a given time, where the signal is spatially coherent and visible by inspection [see Figs. 4(b) and 6(a)]. Some previous work has shown similar performance to the data presented here, e.g., coherent signal over a few hundreds of meters [6], [7]. Other work has detected acoustic sources

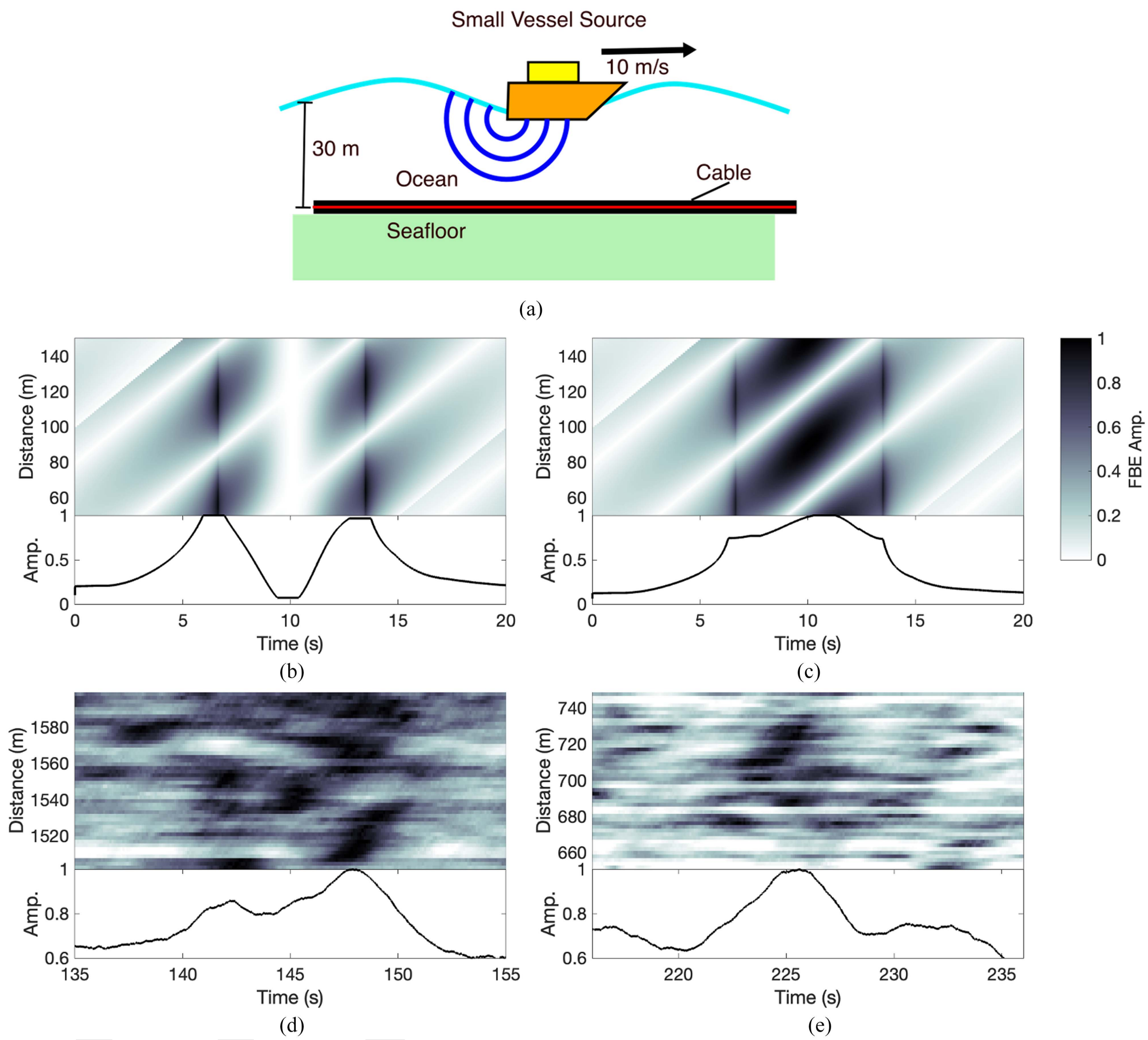

Fig. 7. Synthetic versus observed FBE for suspected buried and unburied fiber on the seafloor. (a) Schematic of moving source model used in the synthetic calculations. Synthetic predictions for FBE for (b) buried and (c) unburied cables on the seafloor. Observed FBE along sections of suspected (d) buried and (c) unburied cables. Top grayscale subpanels in (b)–(e) show the moveout-corrected FBE. In the observed FBE plots, data are the same as shown in Fig. 4(b) for the small vessel pass, using the same frequency band of 60–80 Hz. Time is relative to the top trace, and the other traces are shifted relative to it. Bottom subpanels in (b)–(e) show the sum of the moveout-corrected FBE to highlight the incidence angle sensitivity of the small vessel signals.

at greater distances, several kilometers or more [2], [3], [13], [17]. Possible explanations for differences in detection distances include the power/strength of the sources, propagation efficiency in the water column, coupling of the cable, cable type, or some combination of these factors.

We observe strong variability in sensitivity along the length of the cable. Some of the variability can be attributed to optical polarization-based fading. Fading occurs due to the use of a single optical probe frequency as probe, which can have destructive interference in some parts of the cable. Additional contributions to this noise emanate from variability of the substrate and/or coupling of the fiber to the seabed [38]. The variability along our cable also generally correspond to geological changes along strike of the cable [see Fig. 1(a)]. Specifically, we observe higher amplitude signals from ocean waves where the cable may be predominantly supported by rock outcrop indicated by scarps in the bathymetry and where slopes face the direction of the incoming wavefield. Vessel signals are most prominent on cables sections with smooth, flat topography.

The cable between 1450 and 1800 m, where the vessel signals have the highest amplitudes, may be partially buried by sediment. There is evidence for sediment transport in the region that may have buried the cable in this location. Inspection of the bathymetry (see Fig. 1) reveals the presence of sand waves and scour. This indicates that sediment transport is dynamic in the region due to the high tidal velocities and erosion of the beaches and sedimentary rock formations. Previous studies using submarine cables have also observed sharp changes in cable sensitivity [8] and have also suggested variability in the substrate and changing coupling as the likely cause.

In the suspected buried region of the cable, the FBE appears to have multiple peaks visible, which become more apparent when the FBE is corrected for moveout (see Fig. 7(a), top panel) and summed along distance (see Fig. 7(a), bottom panel). In contrast, for a section of cable at the seafloor (650–750 m), the

FBE appears to have a single peak [see Fig. 7(b)]. This agrees with the predictions in Section II-D. Specifically, the cable in the water column can only be strained via pressure variations, specifically normal stress to cable surface, while a buried cable is subject to normal and shear stresses from the surrounding solid medium (see Section II-D). Overall, our simple model from Section III-B captures much of the characteristics observed in the FBE plots from the suspected buried and unburied cable. The agreement between theory and observation here suggests a simple and inexpensive way to test whether a cable is buried or not using signals from local boat traffic, which is important for protecting the energy transmission system and minimizing thermal interactions with the surrounding environments and ecosystems [1]. This would obviate the need to dive or send a remotely operated vehicle to inspect the cable.

V. Conclusion

In this article, we have demonstrated the capability of electrical cables used in offshore energy generation for use in DAS. These cables were deployed on the seafloor without intentional burial and coupling to the seafloor. The cables are capable of detecting ocean gravity waves propagating toward the coast and reflections. In addition, small craft can be observed and tracked along the cable, and Doppler shifts are observed that are related to the velocities of the small craft. The character of the small craft FBE signal changes along the length of the cable from a single peak in energy to multiple peaks, which can be explained by a change in the burial state of the cable. This later observation provides a means of determining the burial state of the cable.

Acknowledgment

The authors would like to thank the EMEC staff for their support both in-field and, otherwise, during planning and execution of the field campaign at their tidal energy site. The authors would also like to thank Dr. Arthur Hartog and Alexis Constantinos for discussions on preparation and help during execution of the field campaign.

References

[1] J. Lux, M. Olschewski, P. Schäfer, and W. Hill, "Real-time determination of depth of burial profiles for submarine power cables," *IEEE Trans. Power Del.*, vol. 34, no. 3, pp. 1079–1086, Jun. 2019, doi: 10.1109/TPWRD.2018.2881770.

[2] L. Bouffaut et al., "Eavesdropping at the speed of light: Distributed acoustic sensing of Baleen whales in the arctic," *Front. Mar. Sci.*, vol. 9, Jul. 2022, Art. no. 901348, doi: 10.3389/fmars.2022.901348.

[3] W. S. D. Wilcock, S. Abadi, and B. P. Lipovsky, "Distributed acoustic sensing recordings of low-frequency whale calls and ship noise offshore Central Oregon," *JASA Exp. Lett.*, vol. 3, no. 2, Feb. 2023, Art. no. 026002, doi: 10.1121/10.0017104.

[4] R. A. Rørstadbotnen et al., "Simultaneous tracking of multiple whales using two fiber-optic cables in the arctic," *Front. Mar. Sci.*, vol. 10, Apr. 2023, Art. no. 1130898, doi: 10.3389/fmars.2023.1130898.

[5] M. Landrø et al., "Sensing whales, storms, ships and earthquakes using an arctic fibre optic cable," *Sci. Rep.*, vol. 12, no. 1, Nov. 2022, Art. no. 19226, doi: 10.1038/s41598-022-23606-x.

[6] R. Hunt, R. Rogers, and G. Lees, "Listening to your cable with artificial intelligence for asset monitoring," in *Proc. 10th Int. Conf. Insulated Power Cables*, 2019.

[7] D. Rivet, B. de Cacqueray, A. Sladen, A. Roques, and G. Calbris, "Preliminary assessment of ship detection and trajectory evaluation using distributed acoustic sensing on an optical fiber telecom cable," *J. Acoust. Soc. Amer.*, vol. 149, no. 4, pp. 2615–2627, 2021, doi: 10.1121/10.0004129.

[8] A. Ugalde et al., "Noise levels and signals observed on submarine fibers in the Canary Islands using DAS," *Seismol. Res. Lett.*, vol. 93, no. 1, pp. 351–363, 2021, doi: 10.1785/0220210049.

[9] E. F. Williams et al., "Surface gravity wave interferometry and ocean current monitoring with ocean-bottom DAS," *J. Geophys. Res.: Oceans*, vol. 127, no. 5, 2022, Art. no. e2021JC018375, doi: 10.1029/2021JC018375.

[10] N. J. Lindsey, T. C. Dawe, and J. B. Ajo-Franklin, "Illuminating seafloor faults and ocean dynamics with dark fiber distributed acoustic sensing," *Science*, vol. 366, no. 6469, pp. 1103–1107, 2019, doi: 10.1126/science.aay5881.

[11] K. Taweesintananon et al., "Distributed acoustic sensing of ocean-bottom seismo-acoustics and distant storms: A case study from Svalbard, Norway," *Geophysics*, vol. 88, no. 3, pp. B135–B150, 2023, doi: 10.1190/geo2022-0435.1.

[12] H. Xiao et al., "Locating the precise sources of high-frequency microseisms using distributed acoustic sensing," *Geophys. Res. Lett.*, vol. 49, no. 17, 2022, Art. no. e2022GL099292, doi: 10.1029/2022GL099292.

[13] H. Matsumoto et al., "Detection of hydroacoustic signals on a fiber-optic submarine cable," *Sci. Rep.*, vol. 11, no. 1, Feb. 2021, Art. no. 2797, doi: 10.1038/s41598-021-82093-8.

[14] I. Lior et al., "On the detection capabilities of underwater distributed acoustic sensing," *J. Geophys. Res.: Solid Earth*, vol. 126, no. 3, 2021, Art. no. e2020JB020925, doi: 10.1029/2020JB020925.

[15] A. Sladen et al., "Distributed sensing of earthquakes and ocean-solid earth interactions on seafloor telecom cables," *Nat. Commun.*, vol. 10, no. 1, Dec. 2019, Art. no. 5777, doi: 10.1038/s41467-019-13793-z.

[16] E. F. Williams et al., "Distributed sensing of microseisms and teleseisms with submarine dark fibers," *Nat. Commun.*, vol. 10, no. 1, Dec. 2019, Art. no. 5778, doi: 10.1038/s41467-019-13262-7.

[17] K. Taweesintananon, M. Landrø, J. K. Brenne, and A. Haukanes, "Distributed acoustic sensing for near-surface imaging using submarine telecommunication cable: A case study in the Trondheimsfjord, Norway," *Geophysics*, vol. 86, no. 5, pp. B303–B320, 2021, doi: 10.1190/geo2020-0834.1.

[18] G. Marra et al., "Ultrastable laser interferometry for earthquake detection with terrestrial and submarine cables," *Science*, vol. 361, no. 6401, pp. 486–490, 2018, doi: 10.1126/science.aat4458.

[19] T. Worzyk, *Submarine Power Cables (Power Systems)*. Berlin, Germany: Springer, 2009.

[20] N. M. Nasab, J. Kilby, and L. Bakhtiaryfard, "Analysis and design of monopile foundations for offshore wind and tidal turbine structures," *Water*, vol. 14, no. 21, 2022, Art. no. 3555.

[21] T. Asim, S. Z. Islam, A. Hemmati, and M. S. U. Khalid, "A review of recent advancements in offshore wind turbine technology," *Energies*, vol. 15, no. 2, 2022, Art. no. 579.

[22] D. Lande-Sudall, T. Stallard, and P. Stansby, "Co-located offshore wind and tidal stream turbines: Assessment of energy yield and loading," *Renewable Energy*, vol. 118, pp. 627–643, Apr. 2018, doi: 10.1016/j.renene.2017.10.063.

[23] European Marine Energy Centre, 2023. [Online]. Available: https://www.emec.org.uk

[24] UKHO. 2005 HI 1122 Sanday Sound to Westray Firth, 2005. [Online]. Available: https://seabed.admiralty.co.uk/selected-items?x=-304382.19&y=8220780.41&z=11.00

[25] G. E. P. v. 7.3.6.9796, "European Marine Energy Centre, Eday tidal energy test site, 59° 09′54." Accessed: Nov. 2023. [Online]. Available: http://www.google.com/earth/index.html

[26] W. Mykura, *Orkney and Shetland. British Regional Geology*. Edinburgh, U.K.: HMSO, 1976.

[27] A. H. Hartog, *An Introduction to Distributed Optical Fibre Sensors*, 1st ed. Boca Raton, FL, USA: CRC Press, 2017, p. 472.

[28] S. L. Miller and D. G. Childers, *Probability and Random Processes: With Applications to Signal Processing and Communications*, 2nd ed. New York, NY, USA: Academic, 2012.

[29] N. Aghanim et al., "Planck 2018 results," *Astron. Astrophys.*, vol. 641, Sep. 2020, Art. no. A1, doi: 10.1051/0004-6361/201833880.

[30] C. L. Bennett et al., "Nine-year Wilkinson microwave anisotropy probe (Wmap) observations: Final maps and results," *Astrophys. J. Suppl. Ser.*, vol. 208, no. 2, Sep. 2013, Art. no. 20, doi: 10.1088/0067-0049/208/2/20.

[31] B. Budiansky, D. C. Drucker, G. S. Kino, and J. R. Rice, "Pressure sensitivity of a clad optical fiber," *Appl. Opt.*, vol. 18, no. 24, pp. 4085–4088, Dec. 1979, doi: 10.1364/AO.18.004085.

[32] G. K. Batchelor, *An Introduction to Fluid Dynamics* (ser. Cambridge Mathematical Library). Cambridge, U.K.: Cambridge Univ. Press, 2000.

[33] C. Spingys, A. N. Garabato, and M. Belal, "Distributed fibre optic sensing for high space-time resolution ocean velocity observations: A case study from a macrotidal channel," *Earth Space Sci.*, vol. 11, no. 5, May 2024, Art. no. e2023EA003315, doi: 10.5281/zenodo.7896793.

[34] P. Bogiatzis, A. Karamitrou, J. W. Neale, N. Harmon, C. A. Rychert, and M. Srokosz, "Source regions of infragravity waves recorded at the bottom of the equatorial atlantic ocean, using OBS of the PI-LAB experiment," *J. Geophys. Res.: Oceans*, vol. 125, no. 6, 2020, Art. no. e2019JC015430, doi: 10.1029/2019JC015430.

[35] D. Dolenc, B. Romanowicz, P. McGill, and W. Wilcock, "Observations of infragravity waves at the ocean-bottom broadband seismic stations Endeavour (KEBB) and explorer (KXBB)," *Geochem. Geophys. Geosyst.*, vol. 9, no. 5, May 2008, Art. no. Q05007, doi: 10.1029/2008GC001942, 2008.

[36] N. Harmon, T. Henstock, M. Srokosz, F. Tilmann, A. Rietbrock, and P. Barton, "Infragravity wave source regions determined from ambient noise correlation," *Geophys. Res. Lett.*, vol. 39, 2012, Art. no. L04604, doi: 10.1029/2011GL050414.

[37] J. Neale, N. Harmon, and M. Srokosz, "Source regions and reflection of infragravity waves offshore of the U.S.'s Pacific Northwest," *J. Geophys. Res.: Oceans*, vol. 120, no. 9, pp. 6474–6491, 2015, doi: 10.1002/2015JC010891.

[38] N. J. Lindsey, H. Rademacher, and J. B. Ajo-Franklin, "On the broadband instrument response of fiber-optic DAS arrays," *J. Geophys. Res.: Solid Earth*, vol. 125, no. 2, 2020, Art. no. e2019JB018145, doi: 10.1029/2019JB018145.

Nicholas Harmon received the B.A. degree in history and geological sciences from Boston University, Boston, MA, USA, in 2000, and the Ph.D. degree in geophysics from Brown University, Providence, RI, USA, in 2007.

From 2007 to 2009, he was a National Science Foundation RIDGE2000 Postdoctoral Researcher with the Scripps Institution of Oceanography, San Diego, CA, USA. From 2009 to 2017, he was a Lecturer in Geophysics with the University of Southampton, Southampton, U.K., where he was an Associate Professor from 2017 to 2022. In 2022, he joined the Woods Hole Oceanographic Institution, Woods Hole, MA, USA, as a Research Specialist. His research interests include understanding tectonic and earth system processes using ocean bottom seismology, fiber-optic sensing, marine geophysics, and geodynamics.

Mohammad Belal received the B.Sc. degree in physics, statistics and mathematics from Christian College, Lucknow, India, in 2005, the M.Sc. degree in physics (theoretical) from Aligarh University, Aligarh, India, in 2006, the M.Res. degree in experimental soft condensed matter (Polymer Physics) from the University of Reading, Reading, U.K., in 2007, and the Ph.D. degree in optoelectronics from Optoelectronics Research Centre, University of Southampton, Southampton, U.K., in 2011.

Before joining the NOC as a Principal Investigator in 2019, he worked as a Post-Doctoral Researcher with the Optoelectronics Research Centre and the Department of Physics at the University of Southampton. He is an atomic, molecular and optical Physicist. As a Principal Investigator with the National Oceanography Centre, Southampton, he leads the development of the next generation of wide-area dense spatio-temporal distributed monitoring, visualization, and communication platforms, imbedded with intelligence, for use in the marine, maritime, glacial, and urban environments. He holds a visiting Professor position with the Department of Electronic & Computer Science, University of Southampton, U.K. as well as that of an honorary reader with the Mathematical Sciences, University of Liverpool, Liverpool, U.K. His research interests include range of disciplines, e.g., optical fiber sensing, nonlinear fiber and waveguide optics, high-power fiber lasers and amplifiers, optical-atomic-molecular spectroscopy, coherent atomic control, quantum technologies, complex signals processing, machine learning and Big-Data analytics.

Maria-Daphne Mangriotis received the B.A. degree in geology physics/mathematics from Brown University, Providence, RI, USA, in 2002, and the M.Sc. degree in geotechnical engineering and the Ph.D. degree in applied seismology from the University of California, Berkeley, CA, USA, in 2004 and 2009, respectively.

She held postdoctoral and research fellowships with the Institute of Engineering Seismology and Earthquake Engineering, Thessaloníki, Greece, the University of Pavia, Pavia, Italy, Heriot-Watt University, Edinburgh, U.K., and the University of Edinburgh, Edinburgh. She has worked as staff and consultant for the geotechnical engineering industry (Fugro West), oil and gas industry (Chevron, Berkeley Geoimaging), and on wind farm noise characterization (Community Windpower, North Sea Transition Authority). Her research interests include near-surface reservoir-induced seismicity and ocean monitoring using active and passive source techniques applied to seismic and fiber-optic sensing.

Carl Spingys received the B.Sc. degree in mathematics and climate science and the Ph.D. degree in physical oceanography from the University of Liverpool, Liverpool, U.K., in 2012 and 2016, respectively.

He is a Physical Oceanographer with a wide range of expertise on the development and utilization of observational techniques to make inferences about the processes and structure of the ocean on a range of scales. During his Ph.D. research with the University of Liverpool, he developed a methodology to use traditional ocean moorings to make observations of internal tide Stokes' drift. Following his Ph.D., he worked for several years as a Research Fellow with the University of Southampton, Southampton, U.K., where he made a novel and creative use of observational tools to provide new insights. Since 2023, he has been with the National Oceanography Centre, Southampton.

Catherine A. Rychert received the B.A. degree in physics and geophysics (under University Professors' Program) from Boston University, Boston, MA, USA, in 2001, and the M.Sc. and Ph.D. degrees in seismology from Brown University, Providence, RI, USA, in 2004 and 2007, respectively.

From 2007 to 2009, she was a Postdoctoral Researcher with the Scripps Institution of Oceanography, San Diego, CA, USA. From 2009 to 2011, she was a Natural Environment Research Council Fellow with the University of Bristol, Bristol, U.K. She then joined the University of Southampton, where she was a Lecturer of Geophysics from 2011 to 2014 and an Associate Professor of Geophysics from 2014 to 2022. She is currently an Associate Scientist with Tenure with the Woods Hole Oceanographic Institution, Woods Hole, MA. She has given more than 100 invited talks at international conferences and universities and authored nearly 100 papers in international journals. Her work has been featured in many popular news outlets, including two highlights in Discover Magazine's 100 Top Science Stories of the Year. She has also led several seismic field experiments both on land and at sea. Her main research interests include seismically imaging and understanding the tectonic plate, with a focus on a wide range of tectonic environments, global seismic imaging, using novel measurements including distributed acoustic sensing interrogation of fiber-optic cables, and joint solid earth-oceanographic investigations using high-precision pressure gauges and tall moorings to constrain both ocean current rate changes that affect climate change and tectonic plate motions that inform earthquake and tsunamigenic hazards.

Dr. Rychert received the Bullerwell Prize from the British Geophysical Association in 2014 and the Fowler Prize from the Royal Astronomical Society in 2015. She was a Founding Member, Executive Editor, and Chair of the Diversity, Equity, and Inclusion Task Force of *Seismica*.